

# Delayed-Stability Evaluation and Experimental Validation of Grid-Forming Inverter Dynamic Power-Hardware-in-the-Loop Tests

H. G. Oral, K. Prabakar, *Senior Member, IEEE*, D. M. Anand, *Member, IEEE*, S. Ganguly, *Member, IEEE*, and E. Mallada, *Senior Member, IEEE*,

**Abstract**—Sophisticated control algorithms and the expanded functional use cases of grid-forming (GFM) inverters do not have standardized testing protocols, which make their power hardware-in-the-loop (PHIL) validation particularly valuable. But, ensuring stable GFM PHIL tests is challenging as experimental artifacts can be sources of destabilizing excitations for a GFM control loop. In this paper, we present methodologies to address challenges of GFM PHIL tests, and provide numerical analyses and experimental results that validate our approach. We first discuss the choice of empirical parameters, and tuning of closed-loop controllers that improve the stability and tracking performance of GFM PHIL experiments. We then provide analytical and numerical calculations evaluating the robustness of the closed-loop setup to experimental artifacts; particularly to delays, while accounting for destabilizing dynamic modes of the physical PHIL interconnection. Our experimental results validate closed-loop stability and tracking performance of PHIL tests.

**Index Terms**—power hardware-in-the-loop, grid-forming, validation.

## I. INTRODUCTION

Electrical power networks are hosting an increasing proportion of inverter-based resources (IBRs), which primarily operate today in grid-following (GFL) mode [1], wherein the grid-side AC voltage is tracked and current is generated to obtain the desired power output [2]. Alternately, the AC grid voltage can be established in a distributed fashion using grid-forming (GFM) inverters, which regulate their terminal voltage to balance generation and demand while sharing load between IBRs, in turn providing more resilience. Wide-scale deployment of GFM IBRs requires effective functional specifications for closed-loop control as well as for their integration with circuit protection, fault ride-through, and restoration systems. Further development of tools for modeling, simulation, and testing of GFM IBRs is also required to inform system designers and to standardize GFM capabilities and operations [3].

Power-hardware-in-the-loop (PHIL) tests—where *real* inverters interact with digitally simulated grid conditions in real time—are currently the industry benchmark for evaluating GFL inverters [4], [5], and they enable the rapid iteration of test scenarios that is needed to keep pace with innovation in inverter technology [6]. Also, PHIL tests are noted to lead to better technical standards for GFM inverters [7], [8], and

repeatability of these tests is contingent upon the assessment of stability constraints imposed by experimental tools and the hardware under test (HUT). Stability of GFL inverter testing has been studied extensively [9]; however, best practices for that of GFM inverters with droop regulators are still being developed. Developing stability conditions for a GFM inverter PHIL test setup under dynamic conditions is important as fast transients that are considered outside the bandwidth of interest for the experiment can compromise the stability of the setup [10]. For example, electromagnetic transients due to pulse width modulation (PWM) are relevant to PHIL experiments as both the inverter under test and the controlled voltage source have been observed to interact with line dynamics as well as the tracking and sensing loops within the inverters under test [11]. Furthermore, measurement and computation delays inherent to the experimental setup can further degrade stability margins of the GFM inverter control loop.

In this paper, we present numerical analyses and experimental results that validate the stability of GFM inverter PHIL tests. First, we discuss the empirical choice of parameters that yields a stable hardware interconnection for PHIL experiments. Then, we outline our implementation of closed-loop controllers for improving tracking accuracy and mitigating inherent experimental delays. We derive the overall closed-loop dynamics including the GFM inverter droop response, the tracking controller, a reduced-order model of the interconnection line, and measurement and computation delays; and use this model to perform a numerical stability analysis utilizing a frequency domain method for neutral time-delayed systems (NTDS). Our results provide insights into the role of delays in tracking performance and stability of GFM PHIL experiments and qualitatively demonstrate the impact of the line inductance on delay robustness. Finally, we present results from our experiments in various GFM and GFL operational modes that demonstrate the efficacy of our PHIL test setup.

In Section II, we provide preliminaries and describe the key components of our PHIL setup to be analyzed in the sequel for tracking performance and stability. In sections III and IV, we derive our analytical model and present our numerical results. In Section V, we present experimental results that validate our approach. Section VI concludes the paper.

## II. POWER-HARDWARE-IN-THE-LOOP SETUP

The closed-loop operation in a PHIL experiment is illustrated in Figure 1, where measurements from the inverter under

H. G. Oral is with NIST and Johns Hopkins University, {hasangiray.oral@nist.gov, giray@jhu.edu}. K. Prabakar and S. Ganguly are with NLR, {kumaraguru.prabakar, subhankar.ganguly}@nlr.gov. D. M. Anand completed their part of this work while at NIST and Johns Hopkins University and is currently with Electrify America, danand2@jhu.edu. E. Mallada is with Johns Hopkins University, mallada@jhu.edu.

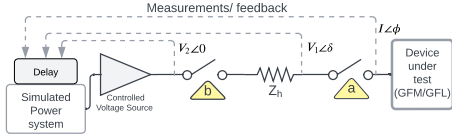


Fig. 1: PHIL setup showing a closed-loop experiment

test are fed back to a model of a power system (shown by dashed lines), which, in turn, is simulated in real time so that the output to the controlled voltage source reflects the grid dynamics of interest. The stability of this two-bus system following a connection event, i.e., closure of breakers a and b, is determined by the GFM inverter droop response—the volt-VAR ( $V_1 - Q$ ) and the frequency-watt ( $\omega - P$ ) dynamic response of the inverter; as well as the coupling impedance,  $Z_h$ , and an infinite bus at frequency  $\omega_0$  with voltage ( $V_2 \angle 0$ ). The interconnection impedance  $Z_h$  is an artifact of the test hardware, and is determined by the electrical connections between the controlled voltage source and the point of interconnection to the inverter under test. This line impedance, once characterized, can be compensated for in the measurements obtained from the experiment; however, it is a significant contributor to the voltage stability conditions of the abstract two-bus power system represented in Figure 1 [12]. The authors in [10] show that stability margins for droop dynamics strongly depend on the interconnection line dynamics if the inductance-to-resistance ratio  $L/R$  is on the same order as the time constant of the nominal AC response. Based on three-phase measurements of our PHIL interconnection impedance  $Z_h$  (see Figure 2),  $R/L \approx 73$  Hz, which is on the same order as the nominal frequency  $f_0 = 60$  Hz. We incorporated this factor into our PHIL setup, as discussed later in this paper.

Delays in the feedback path directly affect the accuracy and stability of this closed-loop system. Common sources of delays include measurement delays associated with the analog to digital conversion and latency caused by the nontrivial computation time needed to simulate the response of a power system; and these sources are abstracted as an aggregate delay in Figure 1. Under steady-state conditions, a common strategy used to compensate for feedback delays is to assume that the delay introduces a corresponding retardation of the voltage angle reference produced by the voltage source,  $V_2 \angle \epsilon$ . Assuming the experiment runs at close-to-nominal grid frequency and experiences near-constant feedback delays, the voltage reference angle,  $\epsilon$ , can be corrected in the software. When performing the dynamic testing of GFL inverters, these delays are characterized as introducing a phase lag in the closed-loop model, and compensation can be applied by inserting an appropriately tuned phase lead [13], [14].

In the sequel, we present the building blocks of our PHIL test setup. As shown in Figure 3, which provides a complete schematic of our closed-loop PHIL experiments, hardware components are mirrored in the digital real-time simulation domain to emulate PHIL testing conditions. The constituents of these two domains are described first. Note that labels *a* and *b* in Figure 1 also refer to the same actuation switches in Figure 3 wherein signal measurement channels are numbered

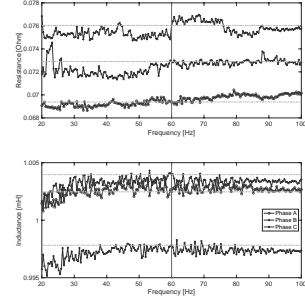


Fig. 2: Resistance and inductance measurements

for reference. We also overview the compensation scheme used for ensuring closed-loop stability and tracking accuracy.

### A. Hardware Setup

*Power-Hardware-Under-Test:* Our work targets a commercially available, off-the-shelf GFM inverter designed to interface fuel cells as the power-hardware-under-test, the output of which is taken from node 1 in Figure 3. The intellectual property of the lower-level control structure is not available for modeling the inverter in a digital real-time simulation; therefore, a PHIL setup needs to be used to evaluate the inverter performance under different modes of operation. A controllable DC supply energizes the inverter under test.

*Controllable DC supply:* We use a DC battery emulator, the Aerovironment AV 900, in constant voltage mode to supply DC power to the fuel cell inverter. Key settings are a voltage set point of 450 V DC (trip voltage is 500 V DC), a DC current limit of 250 A DC, and a power limit of 112.5 kW. These configurations ensure efficient testing and adherence to the fuel cell inverter and laboratory AC and DC bus specifications.

*Grid Emulator - Controllable AC supply:* A controllable AC supply rated at 270 kVA AC is used as the grid emulator and interfaces the inverter at node 7 in Figure 3. The grid emulator receives an analog input that is filtered by the compensation and real-time simulation domains (node 6) and amplifies it to represent the bus voltage of the power system model at node 7. Notably, the grid emulator magnifies a 7 V root-mean-square (RMS) AC voltage to a 300 V RMS AC voltage. We set the protection limit of the grid emulator at 300 V maximum and 150 A for bidirectional current.

At the outset, sound engineering design practices are called for when selecting the controllable voltage source and the corresponding amplifier with regard to their saturation limits, frequency bandwidths, response times, and harmonic distortions. Calibration is often required to address bias in the amplifier gain and to compensate for the input/output impedance of the interface hardware. These experimental considerations are shared among a wide range of PHIL testing applications and are enumerated in standards aimed at improving PHIL testing practices across the industry. A summary of these standardization efforts is presented in [15].

*Series inductor:* The series inductor is a commercial off-the-shelf device with an inductance of 1 millihenry (mH) in each phase (see Figure 2). The series inductor is rated for

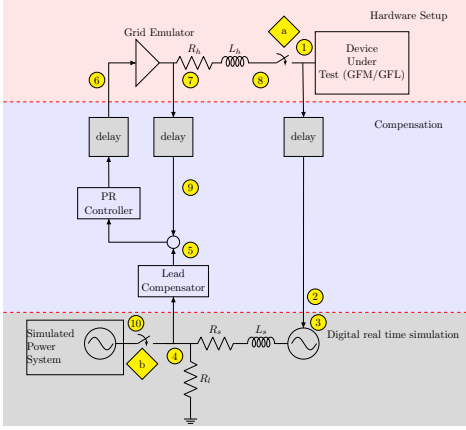


Fig. 3: PHIL laboratory hardware setup

operation of 120 A of current in each phase with a rated line-to-neutral voltage of 277 V (480 V line-to-line RMS). As we will show in the sequel, this inductance value provides a stable interconnection between the inverter and the controllable AC supply and robustness to loop delays during PHIL tests.

### B. Digital Real-Time Simulation (DRTS)

We use a commercial Real-Time Digital Simulator (RTDS) for computations in the simulation domain, which were performed at 50 microseconds ( $\mu s$ ) and at 100  $\mu s$ . These two time steps were taken as examples to demonstrate that the proposed approach works in multiple time step configurations.

*Software model of the power system:* Node 10 in Figure 3 refers to the output of the power system model used in the DRTS platform, which is a simplified microgrid model. We use resistive, inductive, and capacitive loads to represent typical loads in a microgrid system. The series resistance-inductance pair ( $R_s, L_s$ ) used here replicates that of the hardware setup. Further details of DRTS implementation are presented in [14].

### C. Compensation Scheme

As shown in Figure 3, closed-loop operation is sustained by a digital compensation scheme that interconnects the hardware setup to the DRTS domain. The purpose of compensation is two-fold; it is to improve the tracking performance of the grid-emulator and to compensate for loop delays that may degrade stability margins and tracking accuracy.

*Lead Compensator:* A standard lead compensator is used to compensate for loop delays incurred in the simulated grid signal, which is taken at node 4 in Figure 3. This loop delay consists of the delay between nodes 1 and 3 in Figure 3 and computation time due to real-time simulation. Compensator parameters are tuned according to this aggregate delay value.

*Tracking Controller:* Tracking performance is improved using a properly tuned resonant controller [16]. A resonant controller's action on sinusoidal inputs can be interpreted as an analogous integral controller's action on a step input. The goal is to reduce the error between signals 5 and 7 in Figure 3. In addition to reducing tracking error, the resonant controller provides some degree of delay robustness around the nominal operation frequency as we will demonstrate in the sequel.

## III. TRACKING LOOP: DELAY-INDEPENDENT STABILITY

In this section, we investigate the stability of the tracking (resonant controller) loop, which we analyze independently for simplicity, proving delay-independent stability for a frequency interval that contains the nominal operation frequency. The tracking loop is given in Figure 3 between points 5 and 7. The transfer function of the resonant controller is [16]:

$$T_R(s) = \frac{k_R s}{s^2 + b_R s + \omega_0^2},$$

where  $k_R > 0$  is the controller gain, and setting  $b_R$  to a positive value renders a finite bandwidth around the operating frequency,  $\omega_0$ , as  $T(j\omega_0) = \frac{k_R}{b_R}$ . For our application, we set approximately  $\frac{k_R}{b_R} \approx 2f_0 = 120$  Hz. The grid emulator is modeled as a delayed first-order filter [14]:

$$T_{GE}(s) = e^{-s\tau_f} \frac{\omega_g}{s + \omega_g},$$

where  $\omega_g$  is the cutoff frequency, and  $\tau_f$  is an aggregated delay in the forward path that includes grid emulator and real-time simulation delays. The closed-loop transfer function is:

$$\begin{aligned} T_{tracking}(s) &= \frac{T_R(s)T_{GE}(s)}{1 + T_R(s)T_{GE}(s)e^{-s\tau_b}} \\ &= \frac{\omega_g k_R s e^{-s\tau_f}}{(s^2 + b_R s + \omega_0^2)(s + \omega_g) + k_R s \omega_g e^{-s(\tau_f + \tau_b)}}, \end{aligned} \quad (1)$$

where  $\tau_b$  denotes the delay in the feedback. The delay term  $e^{-s\tau_f}$  can be interpreted as an input delay, so it will be lumped into the delay in the simulation, which is addressed by a lead compensator. We evaluate the stability of the tracking loop by computing the characteristic roots of (1). First, we certify the stability as if there was no delay, and then we look for possible imaginary axis crossings of poles due to a delay. Using a standard approach [17], for a practical interval of frequencies, we show that the tracking loop is delay-independent stable. For  $\tau_f = \tau_b = 0$ , the characteristic equation is given by:

$$s^3 + a_2 s^2 + a_1 s + a_0 = 0,$$

where  $a_2 = b_R + \omega_g$ ,  $a_1 = \omega_0^2 + (b_R + k_R)\omega_g$  and  $a_0 = \omega_0^2 \omega_g$ . The roots are on the open left-half plane if and only if  $a_i > 0$  for  $i = 0, 1, 2$  and  $a_2 a_1 > a_0$  (Routh-Hurwitz). All  $a_i$  coefficients are positive, and the latter condition holds because

$$\begin{aligned} (b_R + \omega_g)(\omega_0^2 + (b_R + k_R)\omega_g) &> \omega_0^2 \omega_g, \quad \text{i.e.,} \\ b_R \omega_0^2 + (b_R + k_R)(b_R \omega_g + \omega_g^2) &> 0. \end{aligned}$$

We consider  $\tau_f + \tau_b > 0$  and let  $s = j\omega$  in the characteristic equation of (1) to evaluate imaginary axis crossings of roots:

$$\begin{aligned} c(j\omega) &:= \frac{\omega^2 - (\omega_0^2 + (b_R + k_R)\omega_g)}{k_R \omega_g} + j \frac{\omega_0^2 \omega_g - \omega^2 (b_R + \omega_g)}{k_R \omega_g \omega} \\ &= e^{-j\omega(\tau_f + \tau_b)}. \end{aligned} \quad (2)$$

Note that setting  $\Re(c(j\omega)) < -1$  guarantees that the equality in (2) does not hold because the right-hand side has a magnitude of 1, and therefore no poles cross the imaginary axis. To find an upper bound on  $\omega$  that satisfies this condition, set  $\Re(c(j\omega)) = -1$ , which leads to:

$$\frac{\omega^2 - \omega_0^2}{\omega_g} - b_R = 0 \quad \Rightarrow \quad \omega = \sqrt{\omega_0^2 + b_R \omega_g}.$$

Because  $\Re(c(j\omega))$  is monotonically increasing in  $\omega$ ,  $\Re(c(j\omega)) < -1$  holds if:

$$\omega < \sqrt{\omega_0^2 + b_R \omega_g},$$

which is sufficient for the delay-independent stability of the tracking loop. Note that increasing  $b_R$  trades off tracking accuracy (a smaller open-loop gain at the nominal frequency,  $\omega_0$ ) for delay robustness because the delay-independent stable region can be expanded as  $b_R$  is increased.

#### IV. IMPACT OF LINE DYNAMICS AND INTERFACE DELAY

In this section, we construct a two-voltage source model including transient dynamics of the hardware interconnection line and data transfer delays that arise in the hardware-simulation interface. Under simplifying assumptions, we evaluate closed-loop stability due to line dynamics and delays.

##### A. Power Flow due to Line Dynamics With Delay

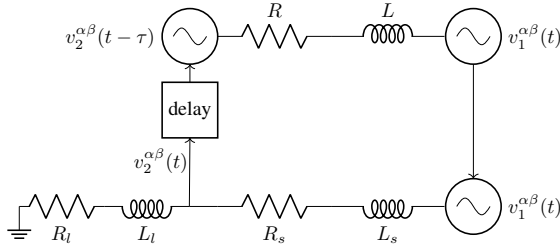


Fig. 4: Hardware simulation interconnection with delay

We define the balanced three-phase voltage signals in the stationary  $\alpha\beta$  coordinates as:

$$v_i^{\alpha\beta}(t) := V_i(t)e^{j\Phi_i(t)} =: v_i(t)e^{j\omega_0 t}, \quad (3)$$

where  $\Phi_i(t) = \phi_i(t) + \omega_0 t$ . Note that the definition in (3) also implies a phasor form given in terms of the phase angle  $\phi_i(t)$  and RMS voltage magnitude,  $V_i(t)$ , as  $v_i(t) = V_i(t)e^{j\phi_i(t)}$ . We assume that the system has a sinusoidal equilibrium expressed as  $\Phi_i(t) \rightarrow \omega_0 t + \phi_i^*$  and  $V_i(t) \rightarrow V_i^*$  as  $t \rightarrow \infty$  with constant  $\phi_i^*$  and  $V_i^*$ . We use this set of definitions for voltage source 1 (the device under test—GFM inverter) and voltage source 2 (grid emulator), which are interconnected with a line with resistance,  $R$ , and inductance,  $L$ , as given in Figure 4. The line dynamics are given by:

$$L \frac{di_{12}^{\alpha\beta}}{dt} = -Ri_{12}^{\alpha\beta}(t) + v_1^{\alpha\beta}(t) - v_2^{\alpha\beta}(t - \tau),$$

where the induced current would be of the form  $i_{12}^{\alpha\beta}(t) := i_{12}(t)e^{j\omega_0 t}$ , and we introduce an input delay,  $\tau$ , to voltage source 2. Then, using the definitions in (3), the line dynamics can be written in a coordinate frame that rotates as  $e^{j\omega_0 t}$ :

$$L \frac{di_{12}}{dt} + (R + j\omega_0 L)i_{12}(t) = v_1(t) - v_2(t - \tau)e^{-j\omega_0 \tau} \quad (4)$$

$$=: \Delta v_{12}(t, \tau)$$

Taking the Laplace transform of (4) gives:

$$i_{12}(s, \tau) = \frac{\Delta v_{12}(s, \tau)}{Ls + R + j\omega_0 L} =: i_{12}^0(s, \tau) \frac{1}{\frac{Ls}{R + j\omega_0 L} + 1},$$

where  $i_{12}^0(s, \tau) = \frac{\Delta v_{12}(s, \tau)}{R + j\omega_0 L}$  is the zeroth-order (quasi-static) phasor current. Using an argument similar to the one in [10], we assume a sufficiently small  $|\frac{Ls}{R + j\omega_0 L}|$  that allows a first-order Taylor approximation:

$$i_{12}(s, \tau) \approx i_{12}^0(s, \tau) \left( 1 - \frac{L}{R + j\omega_0 L} s \right),$$

which can be expressed in the time domain as:

$$\begin{aligned} i_{12}(t, \tau) &\approx \frac{\Delta v_{12}(t, \tau)}{R + j\omega_0 L} - \frac{L}{(R + j\omega_0 L)^2} \frac{d}{dt} \Delta v_{12}(t, \tau) \\ &= \frac{v_1(t) - v_2(t - \tau)e^{-j\omega_0 \tau}}{R + j\omega_0 L} \\ &\quad - \frac{L}{(R + j\omega_0 L)^2} (\dot{v}_1(t) - \dot{v}_2(t - \tau)e^{-j\omega_0 \tau}) \end{aligned}$$

The instantaneous complex power can then be computed as:

$$\begin{aligned} p_{12}(t) &= v_1(t)i_{12}(t)^H \\ &\approx v_1(t) \left[ (G - jB)(v_1(t)^H - v_2(t - \tau)^H e^{j\omega_0 \tau}) \right. \\ &\quad \left. - (G' + jB')(\dot{v}_1(t)^H - \dot{v}_2(t - \tau)^H e^{j\omega_0 \tau}) \right] \\ &= V_1(t) \left[ (G - jB)(V_1(t) - V_2(t - \tau)e^{j\theta_{12}(t, \tau)}) \right. \\ &\quad \left. - (G' + jB')(\dot{V}_1(t) - \dot{V}_2(t - \tau)e^{j\theta_{12}(t, \tau)}) \right. \\ &\quad \left. - jV_1(t)\dot{\phi}_1(t) + jV_2(t - \tau)\dot{\phi}_2(t - \tau)e^{j\theta_{12}(t, \tau)} \right] \quad (5) \end{aligned}$$

where  $\theta_{12}(t, \tau) := \phi_1(t) - \phi_2(t - \tau) + \omega_0 \tau$ , the complex conjugation is denoted by superscript ‘H,’ and we use:

$$\begin{aligned} G &:= \frac{R}{R^2 + \omega_0^2 L^2}, & B &:= -\frac{L\omega_0}{R^2 + \omega_0^2 L^2}, \\ G' &:= \frac{L(R^2 - \omega_0^2 L^2)}{(R^2 + \omega_0^2 L^2)^2}, & B' &:= \frac{2RL^2\omega_0}{(R^2 + \omega_0^2 L^2)^2}. \end{aligned}$$

We then linearize (5) with respect to the variable  $x(t, \tau) = [x_1(t) \ x_2(t - \tau)]^T$  with  $x_i(t) := [\phi_i(t) \ \dot{\phi}_i(t) \ V_i(t) \ \dot{V}_i(t)]$ , and around an equilibrium point  $x^* = [x_1^* \ x_2^*]^T$  with  $x_i = [\phi_i^* \ 0 \ V_i^* \ 0]$ :

$$\begin{aligned} \delta p_{12}(t, \tau, x^*) &=: \delta P_{12}(t, \tau, x^*) + j\delta Q_{12}(t, \tau, x^*) \\ &\approx (\nabla_x p_{12}(t, \tau)|_{x=x^*})^T \delta x(t, \tau) \\ &= \begin{bmatrix} -j(G - jB)V_1^*V_2^*e^{j(\phi_{12}^* + \omega_0 \tau)} \\ j(G' + jB')V_1^{*2} \\ (G - jB)(2V_1^* - V_2^*e^{j(\phi_{12}^* + \omega_0 \tau)}) \\ -(G' + jB')V_1^* \\ j(G - jB)V_1^*V_2^*e^{j(\phi_{12}^* + \omega_0 \tau)} \\ -j(G' + jB')V_1^*V_2^*e^{j(\phi_{12}^* + \omega_0 \tau)} \\ -(G - jB)V_1^*e^{j(\phi_{12}^* + \omega_0 \tau)} \\ (G' + jB')V_1^*e^{j(\phi_{12}^* + \omega_0 \tau)} \end{bmatrix}^T \begin{bmatrix} \delta x_1(t)^T \\ \delta x_2(t - \tau)^T \end{bmatrix}, \quad (6) \end{aligned}$$

where  $\phi_{12}^* := \phi_1^* - \phi_2^*$ ,  $P_{12}$ , and  $Q_{12}$ , respectively, denote the real and reactive power; and ‘ $\delta$ ’ in front of a variable indicates its difference from the equilibrium. Next, we provide the droop dynamics of the GFM inverter under test, due to the first-order approximation of the power flow with a delay in (6).

### B. Droop Dynamics With Line Dynamics and Input Delay

The following assumption, though it restricts our analysis to a fixed real-to-reactive load ratio, provides a reduction in the model order and thereby facilitates gaining useful insight into the stability properties of the GFM inverter testing.

**Assumption 1.** *The respective inductance-to-resistance ratios of the simulated line and the simulated load satisfy  $\frac{L_s}{R_s} \approx \frac{L_l}{R_l}$ .*

We highlight that test cases involving arbitrary values of apparent power are covered by this assumption as long as real and reactive loads scale according to the fixed ratio. For simplicity, we choose the phase angle equilibrium points as  $\phi_{12}^* = 0$ , which, together with Assumption 1, leads to  $V_2^* = \gamma V_1^*$ ,  $\delta V_2 \approx \gamma \delta V_1$  and  $\delta \phi_2 \approx \delta \phi_1$ , where  $\gamma = \frac{R_l}{R_s + R_l}$  (derivation is omitted for brevity). After substituting for these variables (and dropping the subscript index for the inverter parameters), taking  $V^* = V_b$  (1 per unit (pu)), and normalizing the voltage magnitude as  $\delta U = \frac{\delta V}{V_b}$ , where  $V_b$  denotes the base voltage magnitude, we state the per-unit power expressions as:

$$\delta P_{pu}(t, \tau) \approx \begin{bmatrix} -\gamma(B \cos(\omega_0 \tau) - G \sin(\omega_0 \tau)) \\ -B' \\ G(2 - \gamma \cos(\omega_0 \tau)) - B\gamma \sin(\omega_0 \tau) \\ -G' \\ \gamma(B \cos(\omega_0 \tau) - G \sin(\omega_0 \tau)) \\ \gamma(B' \cos(\omega_0 \tau) + G' \sin(\omega_0 \tau)) \\ -\gamma(G \cos(\omega_0 \tau) + B \sin(\omega_0 \tau)) \\ \gamma(G' \cos(\omega_0 \tau) - B' \sin(\omega_0 \tau)) \end{bmatrix}^T \begin{bmatrix} \delta \phi(t) \\ \delta \dot{\phi}(t) \\ \delta U(t) \\ \delta \dot{U}(t) \\ \delta \phi(t - \tau) \\ \delta \dot{\phi}(t - \tau) \\ \delta U(t - \tau) \\ \delta \dot{U}(t - \tau) \end{bmatrix} \quad (7a)$$

$$\delta Q_{pu}(t, \tau) \approx \begin{bmatrix} -\gamma(G \cos(\omega_0 \tau) + B \sin(\omega_0 \tau)) \\ G' \\ -B(2 - \gamma \cos(\omega_0 \tau)) - G\gamma \sin(\omega_0 \tau) \\ -B' \\ \gamma(G \cos(\omega_0 \tau) + B \sin(\omega_0 \tau)) \\ -\gamma(G' \cos(\omega_0 \tau) - B' \sin(\omega_0 \tau)) \\ \gamma(B \cos(\omega_0 \tau) - G \sin(\omega_0 \tau)) \\ \gamma(B' \cos(\omega_0 \tau) + G' \sin(\omega_0 \tau)) \end{bmatrix}^T \begin{bmatrix} \delta \phi(t) \\ \delta \dot{\phi}(t) \\ \delta U(t) \\ \delta \dot{U}(t) \\ \delta \phi(t - \tau) \\ \delta \dot{\phi}(t - \tau) \\ \delta U(t - \tau) \\ \delta \dot{U}(t - \tau) \end{bmatrix} \quad (7b)$$

By an abuse of notation, line parameters  $B$ ,  $G$ ,  $B'$ , and  $G'$  are given as per-unit quantities in the equation above. Next, we introduce  $d_p = \frac{k_p \omega_0}{S_b}$ ,  $d_q = \frac{k_q V_b}{S_b}$ , where  $k_p$  and  $k_q$  denote the per-unit droop gains, and  $S_b$  denotes the base apparent power. Then, the closed-loop expressions for the inverter droop dynamics can be restated as:

$$\begin{aligned} \delta \dot{\phi}(t) &\approx \delta \omega(t) \\ \sigma \delta \dot{\omega}(t) &\approx -\delta \omega(t) - k_p \omega_0 \delta P_{pu}(t, \tau) \\ \sigma \delta \dot{U}(t) &\approx -\delta U(t) - k_q \delta Q_{pu}(t, \tau) \end{aligned}$$

Rearranging these expressions in matrix form, we obtain:

$$N_0 \dot{z}(t) \approx N_1(\tau) \dot{z}(t - \tau) + M_0(\tau) z(t) + M_1(\tau) z(t - \tau)$$

where:  $z(t) := [\delta \phi(t) \quad \delta \omega(t) \quad \delta U(t)]^T$  and:

$$\begin{aligned} N_0 &= \begin{bmatrix} 1 & 0 & 0 \\ 0 & \sigma & -k_p \omega_0 G' \\ 0 & 0 & \sigma - k_q B' \end{bmatrix} \\ N_1(\tau) &= \begin{bmatrix} 0 & 0 & 0 \\ 0 & 0 & -k_p \omega_0 \gamma (G' \cos(\omega_0 \tau) - B' \sin(\omega_0 \tau)) \\ 0 & 0 & -k_q \gamma (B' \cos(\omega_0 \tau) + G' \sin(\omega_0 \tau)) \end{bmatrix} \\ M_0(\tau) &= \begin{bmatrix} 0 & 1 \\ k_p \omega_0 \gamma (B \cos(\omega_0 \tau) - G \sin(\omega_0 \tau)) & k_p \omega_0 B' - 1 \\ k_q \gamma (G \cos(\omega_0 \tau) + B \sin(\omega_0 \tau)) & -k_q G' \end{bmatrix} \\ M_1(\tau) &= \begin{bmatrix} 0 & 0 & 0 \\ -k_p \omega_0 \gamma (B \cos(\omega_0 \tau) - G \sin(\omega_0 \tau)) & -k_p \omega_0 [G(2 - \gamma \cos(\omega_0 \tau)) - B\gamma \sin(\omega_0 \tau)] & -1 + k_q [B(2 - \gamma \cos(\omega_0 \tau)) + G\gamma \sin(\omega_0 \tau)] \\ -k_q \gamma (G \cos(\omega_0 \tau) + B \sin(\omega_0 \tau)) & -k_p \omega_0 \gamma (B' \cos(\omega_0 \tau) + G' \sin(\omega_0 \tau)) & k_p \omega_0 \gamma (G \cos(\omega_0 \tau) + B \sin(\omega_0 \tau)) \\ 0 & k_q \gamma (G' \cos(\omega_0 \tau) - B' \sin(\omega_0 \tau)) & -k_q \gamma (B \cos(\omega_0 \tau) - G \sin(\omega_0 \tau)) \end{bmatrix}. \quad (8) \end{aligned}$$

This differential equation represents a neutral time-delayed system (NTDS) because a delayed argument appears for derivative terms in addition to non-derivative terms, i.e.,  $N_1(\tau) \neq 0$  and  $M_1(\tau) \neq 0$ . Time-delayed systems have transcendental characteristic equations and therefore infinitely many characteristic roots, and, in general, an analytical stability assessment is difficult. But numerical techniques are available for stability assessment of NTDS.

### C. Delay-Dependent Stability Assessment

One numerical technique for the stability assessment of NTDS is a frequency-domain method called the *direct method* [18]. This method relies on Rekasius substitution:

$$e^{-s\tau} = \frac{1 - sT}{1 + sT}, \quad s = j\omega, \quad \omega \in \mathbb{R}, \quad \tau > 0, \quad T \in \mathbb{R}$$

which maps the transcendental characteristic polynomial with infinitely many roots:

$$\det(sI - A_0(\tau) - [A_1(\tau) + sA_2(\tau)]e^{-s\tau}) = 0 \quad (9)$$

where  $A_0(\tau) = N_0^{-1}M_0(\tau)$ ,  $A_1(\tau) = N_0^{-1}M_1(\tau)$  and  $A_2(\tau) = N_0^{-1}N_1(\tau)$ , to a rational polynomial with a finite number of roots:

$$\det\left(sI - A_0(T) - [A_1(T) + sA_2(T)]\frac{1 - sT}{1 + sT}\right) = 0. \quad (10)$$

By an abuse of notation we use matrices  $A_i$  but express them as a function of  $T$  instead of  $\tau$  in (10). This change in variables in  $A_i$ , which is also due to the Rekasius substitution, will be made explicit in the sequel. Note that the Rekasius substitution is performed only for roots on the imaginary axis, and it is an *exact* substitution, not an approximation. The goal is not to

calculate a complete set of roots (as there are infinitely many) but to calculate imaginary axis roots from which stability-instability transitions can be inferred. Rekasius substitution reparametrizes the complex exponential (unit circle) that has angle  $-\omega\tau$  so that it is expressed as a rational polynomial in  $s = j\omega$  of degree 1 with coefficients in  $T$ . The direct method was originally applied to a class of systems for which matrices  $A_i$  are constant. Nevertheless, the method can be extended in a straightforward way by performing the following substitutions in matrices  $A_i(\tau)$  because dependence on  $\tau$  in (8) is only through trigonometric functions:

$$\cos(\omega_0\tau) = \frac{1 - \omega_0^2 T^2}{1 + \omega_0^2 T^2} \quad \text{and} \quad \sin(\omega_0\tau) = \frac{2\omega_0 T}{1 + \omega_0^2 T^2}$$

which are obtained by taking the real and the imaginary parts of the Rekasius substitution and evaluating at  $\omega = \omega_0$ . This way, the polynomial coefficients in (10) can be obtained as functions of  $T$  only.

Then, the imaginary axis roots of (10), which are expressed in terms of  $T$ , are precisely those of (9), which are expressed in terms of  $\tau$ . Because roots are continuous functions of the polynomial coefficients and thus delay  $\tau$ , we are only interested in detecting the imaginary axis roots as their existence indicates a crossing between the left-hand plane and the right-hand plane, i.e., a transition between the stable and the unstable regions. For any imaginary axis root (frequency  $\omega$ ), the following relationship holds due to the Rekasius substitution:

$$\tau = \frac{2}{\omega} [\tan^{-1}(\omega T) + l\pi] \quad (11)$$

where  $l$  is any integer such that  $\tau > 0$ . Using (11), the critical delay value for which the system undergoes a stability transition can be recovered; therefore, critical frequencies and positive delay values for all stability transitions for a given system, whether the system is delay-free stable or not, can be computed using the direct method. For HIL purposes, we are only interested in the system being delay-free stable and computing the smallest positive delay value that would destabilize the system; therefore, we seek the smallest  $l$  value such that  $\tau > 0$  in (11) for any candidate pair of  $\omega$  and  $T$ .

We implement direct method based on the procedural steps given in [18], to which the reader should refer for further details. Evaluating (10) leads to a 6<sup>th</sup>-order polynomial equation in  $s$  where the real coefficients are polynomials in  $T$ . The polynomial equation is then immediately reduced to a 5<sup>th</sup>-order by eliminating the trivial root at  $s = 0$  (a marginally stable pole due to the phase angle drift). Then, the first column of a Routh array is constructed using coefficients of the polynomial in  $s$ , which yields rational polynomials in  $T$  as array entries. Because the number of sign changes on the first column of a Routh array equals the number of right-hand plane poles, any real zero of array entries (as rational polynomials reduced to the lowest terms) is a candidate value for  $T$  for which there is an imaginary axis crossing (recall that  $T \in \mathbb{R}$ ). For each candidate  $T$  value, the imaginary axis roots of (10) are computed, resulting in pairs  $(\omega, T)$  that lead to a critical positive-delay value computed via (11). Noting again that we assume delay-free stability, we then take the minimum

Parameter	Description	Value
$V_b$	Base RMS dq-voltage magnitude	270 V
$S_b$	Base apparent power	10 kVA
$\omega_0$	Nominal frequency	$120\pi$ rad/s
$\sigma^{-1}$	Power measurement filter frequency	$12\pi$ rad/s
$R$	Line resistance	0.073 $\Omega$
$L$	Line inductance	$\{0, 10^{-3}, 10^{-2}, 10^{-1}, 1\}$ mH
$\gamma$	Feedback constant	0.5

TABLE I: Parameter values for numerical calculations

over all  $(\omega, T)$  pairs of the critical positive-delay values for which system undergoes a stability transition. This value is the smallest destabilizing positive-delay value.

#### D. Numerical Results

Parameter values used in numerical calculations, which are typical values drawn from the literature, are given in Table I. We use  $\gamma = 0.5$  in numerical calculations because this value provides an operating point at which the power injected by the inverter is maximally absorbed by the grid emulator. For four scenarios in which inductance values are an order of magnitude apart; and for a scenario with no inductance, we numerically calculate the smallest critical positive-delay value that destabilizes a delay-free-stable system for various values of per-unit droop gain pair  $(k_p, k_q)$ . Each scenario is given as a color map in Figures 5b to 5f. The particular region of  $(k_p, k_q)$  is defined in each scenario based on the delay-free stability regions given for various inductance values in Figure 5a.

Some notable observations from Figure 5a are as follows. For  $L \in \{2 \times 10^{-5}, 10^{-4}, 10^{-3}, 10^{-2}\}$  mH, the delay-free stability regions monotonically shrink as the inductance value increases. The boundary of these regions allows for an arbitrarily large value for one droop gain for a sufficiently small value of (at the expense of) the other droop gain. This behavior is more pronounced for larger inductance values in this set. These relatively small values of inductance result in unbounded delay-free stability regions, whereas at  $L = 10^{-1}$  mH, the stability region is the smallest relative to that of all other scenarios in Figure 5a and is a bounded one. Beyond this inductance value, specifically for  $L \in \{1, 1.1\}$  mH, bounded stability regions monotonically grow. The smallest stability region is induced by a value of  $L$ , which is in the neighborhood of  $10^{-1}$  mH. Typical values of per-unit droop gains  $k_p$  and  $k_q$  are on the order of  $10^{-3}$  and  $10^{-2}$ , respectively [19]; therefore, stability margins for the scenario of  $L = 10^{-1}$  mH (or smaller) could be limiting for HIL experiments. It could be argued that  $L < 10^{-2}$  mH suffices in the absence of a delay, but as will be shown in the sequel, a sufficiently large inductance is needed to improve the stability margins of delayed operation. A line inductance of  $L = 1$  mH, which is only one order of magnitude larger than the value that gives the smallest stability region, is chosen for the experimental setup, which, per the numerical calculations, can provide a sufficient stability margin for delay-free operation.

Each color map in Figures 5b to 5f contains empty regions for sufficiently small values of droop gains. These regions contain points  $(k_p, k_q)$  for which the system is *delay-independent* stable, i.e., a delay-free stable system (stable for  $\tau = 0$ ) is stable for any  $\tau > 0$ . For the inductance value  $L = 1$  mH that is used in the experiments, this delay-independent stable

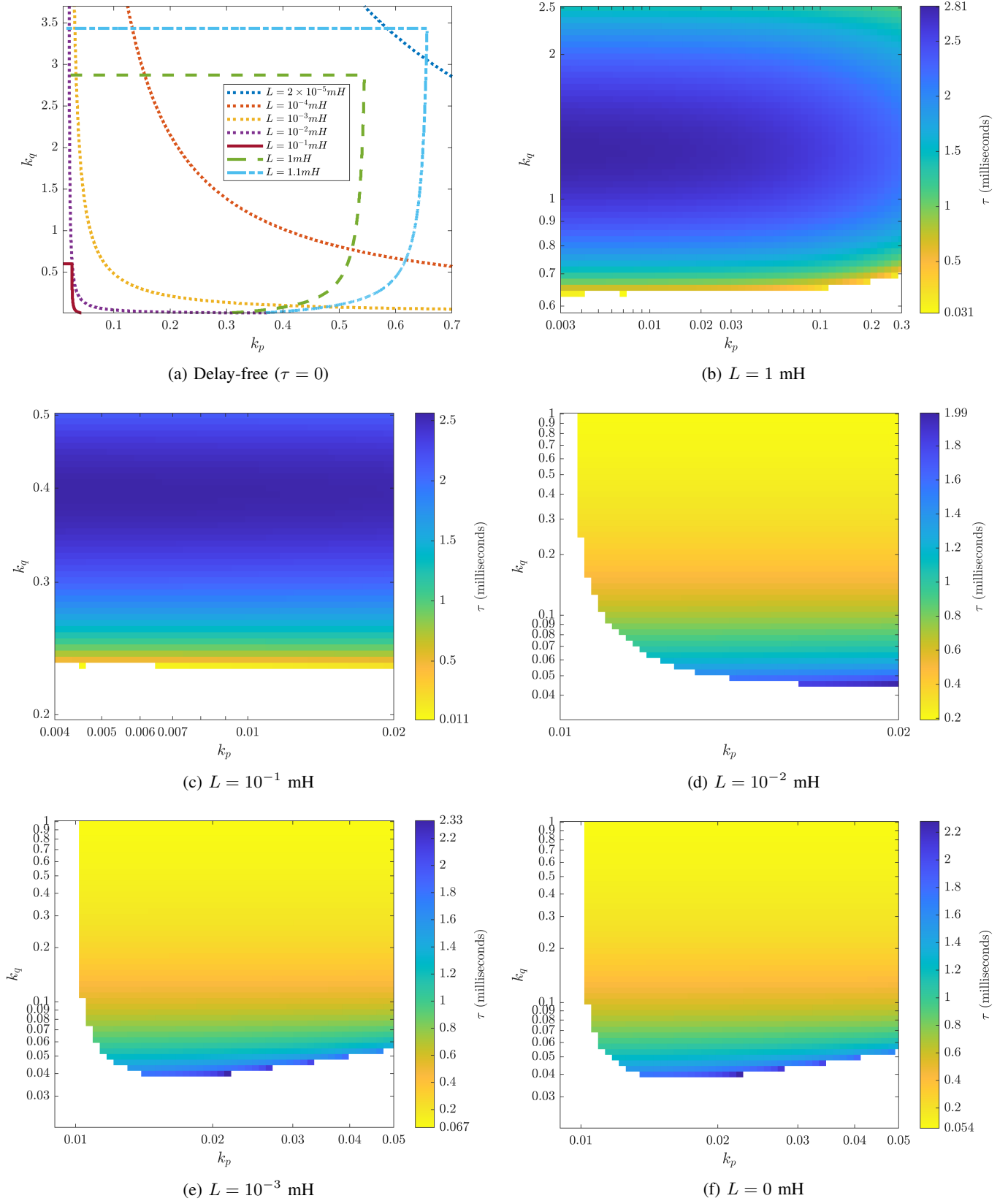


Fig. 5: (a) Delay-free stability regions for various inductance values. (b–f) Color map of critical destabilizing positive-delay values for each scenario with a different inductance value. Empty regions in the color maps indicate delay-independent stability, i.e., a delay-free stable (stable for  $\tau = 0$ ) system is stable for any  $\tau > 0$ .

region in Figure 5b, which is upper bounded approximately at voltage droop gain  $k_q = 0.6$  pu (an order of magnitude larger than typical values) and frequency droop gain  $k_p = 0.3$  pu (two orders of magnitude larger than typical values), provides a practically more useful operating region than that of other scenarios. Particularly, for  $L = 10^{-1}$  mH, the delay-independent stable region upper bound is around  $k_q = 0.2$  pu, as shown in Figure 5c with  $k_p < 0.02$  pu. Figures 5d to 5f indicate for the respective values of  $L \in \{10^{-2}, 10^{-3}, 0\}$  mH that this upper bound is around  $k_q = 0.04$  pu (an order of magnitude smaller than that of the case  $L = 1$  mH) for  $k_p$  on the order of 0.01 pu, unless the frequency droop gain is reduced to  $k_p < 0.01$  pu. These observations suggest that a larger inductance value provides delay robustness from the perspective of achieving a larger delay-independent stable region. Particularly for droop gains  $k_p < 0.3$  pu and  $k_q < 0.6$  pu, the upper bounds of which are at least an order of magnitude larger than the typical values,  $L = 1$  mH provides delay-independent stability. This is the primary benefit of using this inductance value.

In fact, the delay-independent stable region for  $L = 1$  mH in Figure 5b covers the entire region in Figure 5c for  $L = 10^{-1}$  mH and the regions defined by  $k_q < 0.6$  pu in Figures 5d to 5f for the respective inductance values of  $L \in \{10^{-2}, 10^{-3}, 0\}$  mH. In other words,  $L = 1$  mH ensures delay-independent stability for the practical gain values for which smaller inductance values lead to a critical destabilizing value of delay. Outside this region, Figure 5b shows that for  $0.6 \text{ pu} < k_q < 1 \text{ pu}$ ,  $L = 1$  mH produces critical delay values satisfying approximately  $0.031 \text{ ms} < \tau < 2.5 \text{ ms}$ . In the same  $k_q$  interval, for  $k_p > 0.01$  pu, inductance values  $L \in \{10^{-2}, 10^{-3}, 0\}$  mH lead to respective critical delay values of  $\tau \in \{0.2, 0.067, 0.054\}$  ms, and for  $k_p < 0.01$  pu, these inductance values lead to delay-independent stability, as shown in Figures 5d to 5f. The most restrictive range of critical delay values that  $L = 1$  mH produces is at the boundary of the delay-independent and delay-dependent stability regions in Figure 5b (counterintuitively for relatively smaller droop gains), which is  $0.031 \text{ ms} < \tau < 0.5 \text{ ms}$ . The smallest critical delay value in this range is inferior to  $\tau = 0.2$  ms, which  $L = 10^{-2}$  mH produces (for  $0.6 \text{ pu} < k_q < 1 \text{ pu}$  and  $k_p > 0.01$  pu) by an order of magnitude, but it is comparable to the values induced by  $L \in \{10^{-3}, 0\}$  mH. Further, in Figure 5b ( $L = 1$  mH), the critical delay on the delay-independent/delay-dependent stability region boundary mostly attains values on the order of hundreds of  $\mu\text{s}$ , which is comparable to or better than the critical delay values of  $\tau \in \{0.2, 0.067, 0.054\}$  ms produced by  $L \in \{10^{-2}, 10^{-3}, 0\}$  mH (for  $0.6 \text{ pu} < k_q < 1 \text{ pu}$ , and  $k_p > 0.01$  pu), as shown in Figures 5d to 5f; therefore, for relatively large droop gains  $k_p > 0.01$  pu and  $k_q > 0.6$  pu (at least one order of magnitude larger than typical values),  $L = 1$  mH still performs comparably to the smaller inductance values  $L \in \{10^{-2}, 10^{-3}, 0\}$  mH.  $L = 1$  mH underperforms only if  $k_p < 0.01$  pu and  $k_q > 0.6$  pu, which leads to delay-independent stability for smaller inductance values of  $L \in \{10^{-2}, 10^{-3}, 0\}$  mH. Yet, this operating region would be less common because it requires the voltage droop gain to attain values that are an order of magnitude larger than typical; whereas the frequency droop gain is limited to typical

values, which would imply larger reactive power deviations with respect to nominal compared to those of real power.

The ranges of critical destabilizing delay values are comparable in all scenarios. For larger values of inductance  $L \in \{1, 10^{-1}\}$  mH, the most restrictive critical delay value emerges for relatively smaller values of voltage droop gain  $k_q$ , as shown in Figures 5b and 5c. This critical delay value then improves for larger  $k_q$  before it degrades again, as the boundary of delay-free stability regions is approached (see Figure 5a). In contrast, critical delay values induced by smaller values of inductance  $L \in \{10^{-2}, 10^{-3}, 0\}$  mH are most restrictive for larger values of voltage droop gain  $k_q$ , and they improve for smaller values of this gain, as shown in Figures 5d to 5f. We note that critical delay values are relatively more sensitive to voltage droop gain,  $k_q$ , than to frequency droop gain,  $k_p$ , for all scenarios, which could be due to our simplifying assumption of using a real feedback constant, e.g., stronger dependence on voltage magnitude dynamics; however, delay-independent stability regions are still sensitive to frequency droop gain,  $k_p$ , for smaller values of inductance  $L \in \{10^{-2}, 10^{-3}, 0\}$  mH, as shown in Figures 5d to 5f.

Although  $L = 1$  mH provides the highest degree of robustness via a large delay-independent stability region, smaller inductance values can also be sufficient, depending on the application and keeping in mind the associated stability margin deficit. For example,  $k_q < 0.2$  pu and  $k_p < 0.02$  pu, which allows droop gains of one order of magnitude larger than typical, is a delay-independent stability region in Figure 5c for  $L = 10^{-1}$  mH; however, upper bounds of the delay-free stability region in this scenario are also on the same order (see Figure 5a), which is more restrictive than that of  $L \in \{1, 10^{-2}, 10^{-3}, 0\}$  mH. An almost full range of critical destabilizing delay values in scenarios of  $L \in \{10^{-2}, 10^{-3}, 0\}$  mH is contained in the region  $k_q < 0.2$  pu and for  $k_p$  on the order of 0.01 pu. For these smaller inductance values, for example, critical delay values of 1 ms or better can be achieved for voltage droop gain  $k_q < 0.06$  pu (allows up to typical values), or 0.6 ms or better can be achieved for  $k_q < 0.1$  pu (allows up to one order of magnitude larger than typical), whereas the frequency droop gain can be chosen as large as on the order of 0.01 pu (one order of magnitude larger than typical). Noting that the simulation delay is approximately 0.05–0.1 ms, well-tuned lag compensation can manage delays.

## V. EXPERIMENTAL RESULTS

This section presents the PHIL experimental results. First, we present the results from controlling the grid emulator voltage using the resonant tracking controller. Then, we present the results from operating the inverter under GFM and GFL modes of operation depending on the microgrid mode.

### A. Voltage Tracking

Figure 6 shows three waveforms. The first waveform is the voltage feedback, the second shows the voltage set point, and the third shows the voltage error. Before the resonant controller is turned on, the grid simulator is not following the voltage set point. After turning on the resonant controller,

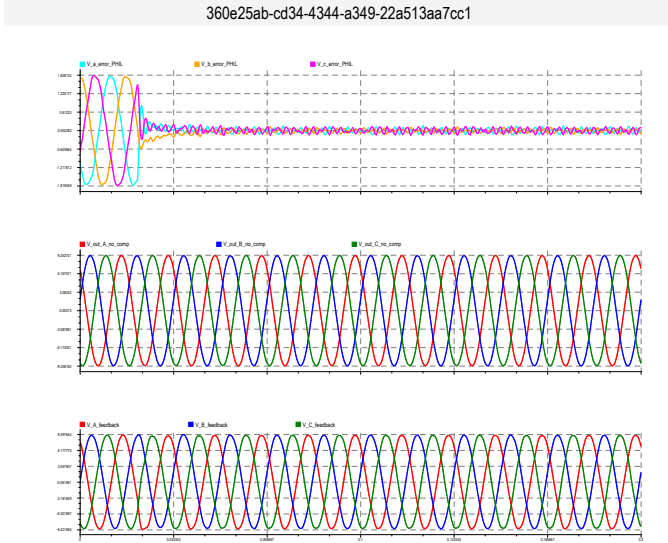


Fig. 6: Operation of the grid simulator with the error minimized when the proportional resonant controller is activated

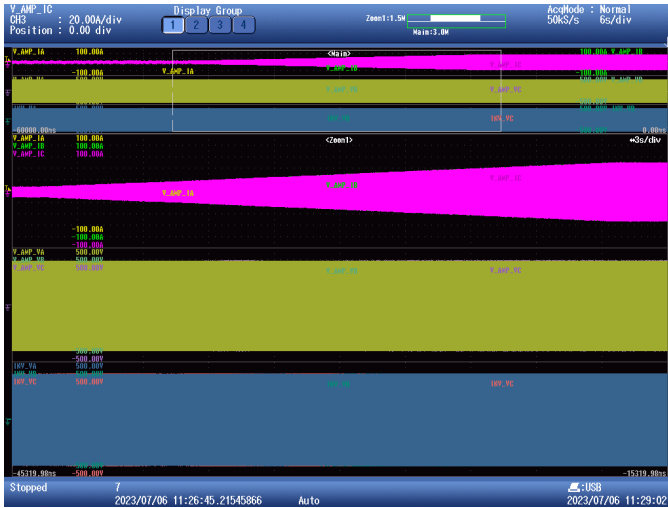


Fig. 7: Grid-connected dispatch

the grid simulator can track the voltage, and the tracking error is significantly reduced.

### B. Power Tracking

*Grid-connected dispatch with inverter in GFL mode:* Figure 7 shows the results from grid-connected dispatch with the inverter in GFL mode of operation.

*Grid-connected mode to islanded mode with inverter transitioning from GFL to GFM mode:* Figure 8 shows the results when the microgrid transitions from grid-connected mode to islanded mode. During this transition, the inverter switched from GFL mode to GFM mode.

*Islanded mode of operation with inverter in GFM mode of operation:* Figure 9 shows the results when the microgrid is in islanded mode of operation. In islanded mode, loads in the microgrid were increased in steps. The inverter operated in GFM mode and supported the load steps.

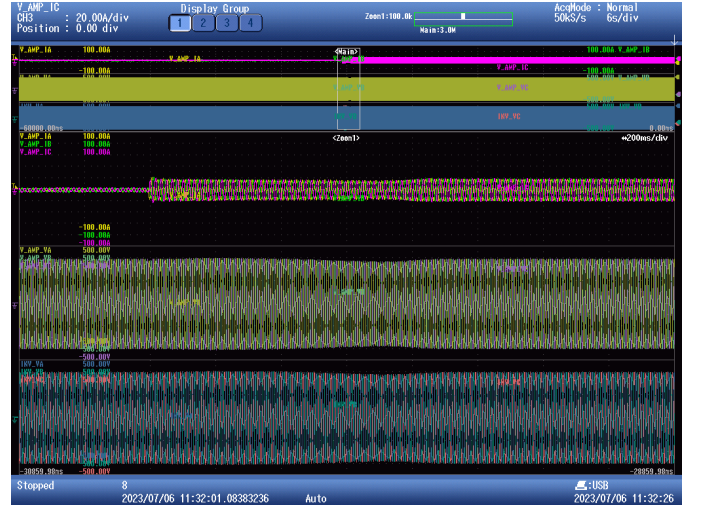


Fig. 8: Transition of microgrid from grid-connected mode to islanded mode. The inverter transitions from GFL mode to GFM mode.

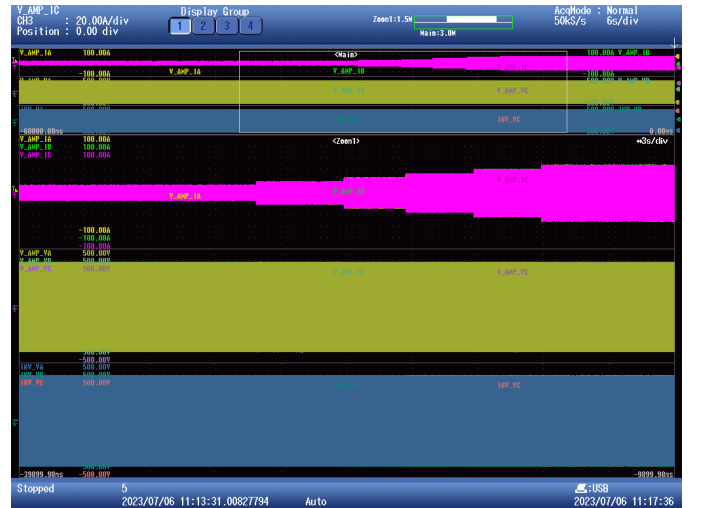


Fig. 9: Islanded dispatch—inverter in GFM mode supporting loads in the microgrid (microgrid is in islanded mode)

*Grid resynchronization transition with inverter transitioning from GFM mode to GFL mode:* Figure 10 shows the results when the microgrid transitions from islanded mode to grid-connected mode of operation. During this transition, the inverter transitions from GFM mode to GFL mode of operation.

## VI. CONCLUSION

This paper addressed challenges of ensuring the stability of GFM PHIL tests under dynamic conditions; via the use of lead compensation and resonant tracking control schemes as well as the appropriate choice of PHIL interconnection parameter values. These challenges, particularly pertaining to loop delays and destabilizing dynamic modes of PHIL interconnections, have been analyzed using analytical models and numerical simulations. The efficacy of our delay compensation and tracking control approaches has been demonstrated in PHIL

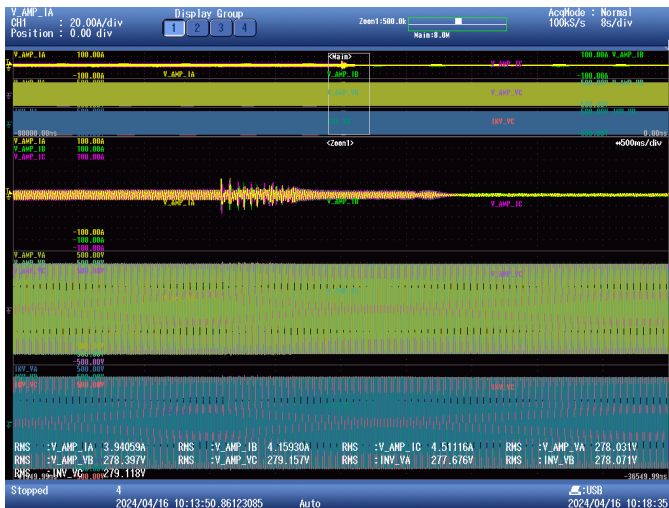


Fig. 10: Transition of microgrid from islanded mode to grid-connected mode. The inverter transitions from GFM mode to GFL mode.

experiments at high power (100 kVA GFM inverter) and in various dynamic modes.

#### ACKNOWLEDGMENTS

This work was authored in part by the National Laboratory of the Rockies (NLR) for the U.S. Department of Energy (DOE) under Contract No. DE-AC36-08GO28308 and the National Institute of Standards and Technology (NIST). Funding for the NLR author provided by the U.S. Department of Energy Office of Energy Efficiency and Renewable Energy Hydrogen and Fuel Cell Technologies Office. The views expressed in the article do not necessarily represent the views of the DOE or the U.S. Government. Certain commercial entities, equipment, or materials may be identified in this document to describe an experimental procedure or concept adequately. Such identification is not intended to imply recommendation or endorsement by the National Institute of Standards and Technology, nor is it intended to imply that the entities, materials, or equipment are necessarily the best available for the purpose. The U.S. Government retains and the publisher, by accepting the article for publication, acknowledges that the U.S. Government retains a nonexclusive, paid-up, irrevocable, worldwide license to publish or reproduce the published form of this work, or allow others to do so, for U.S. Government purposes. Unless otherwise noted, the NIST work was funded solely by the U.S. Government.

#### REFERENCES

- [1] R. Teodorescu, M. Liserre, and P. Rodriguez, *Grid converters for photovoltaic and wind power systems*. Chichester, West Sussex: Wiley, 2011.
- [2] S. Golestan, J. M. Guerrero, and J. C. Vasquez, "Three-Phase PLLs: A Review of Recent Advances," *IEEE Transactions on Power Electronics*, vol. 32, pp. 1894–1907, Mar. 2017.
- [3] Y. Lin, J. Eto, B. Johnson, J. Flicker, R. Lasseter, H. Villegas Pico, G.-S. Seo, B. Pierre, and A. Ellis, "Research Roadmap on Grid-Forming Inverters," Tech. Rep. NREL/TP-5D00-73476, 1721727, MainId:6978, NREL, Nov. 2020.
- [4] G. Lauss, M. O. Faruque, K. Schoder, C. Dufour, A. Viehweider, and J. Langston, "Characteristics and Design of Power Hardware-in-the-Loop Simulations for Electrical Power Systems," *IEEE Transactions on Industrial Electronics*, vol. 63, pp. 406–417, Jan. 2016.
- [5] B. M. Wilamowski and J. D. Irwin, *The industrial electronics handbook. Control and mechatronics*. Boca Raton, FL: CRC Press, 2nd ed ed., 2011. OCLC: 723940296.
- [6] X. Guillaud, M. O. Faruque, A. Tenenge, A. H. Hariri, L. Vanfretti, M. Paolone, V. Dinavahi, P. Mitra, G. Lauss, C. Dufour, P. Forsyth, A. K. Srivastava, K. Strunz, T. Strasser, and A. Davoudi, "Applications of Real-Time Simulation Technologies in Power and Energy Systems," *IEEE Power and Energy Technology Systems Journal*, vol. 2, pp. 103–115, Sept. 2015.

- [7] J. Montoya, R. Brandl, K. Vishwanath, J. Johnson, R. Darbali-Zamora, A. Summers, J. Hashimoto, H. Kikusato, T. S. Ustun, N. Ninad, E. Apablaza-Arancibia, J.-P. Bérrard, M. Rivard, S. Q. Ali, A. Obushevs, K. Heussen, R. Stanev, E. Guillo-Sansano, M. H. Syed, G. Burt, C. Cho, H.-J. Yoo, C. P. Awasthi, K. Wadhwa, and R. Bründlinger, "Advanced Laboratory Testing Methods Using Real-Time Simulation and Hardware-in-the-Loop Techniques: A Survey of Smart Grid International Research Facility Network Activities," *Energies*, vol. 13, p. 3267, June 2020.
- [8] A. Haddadi, M. Zhao, I. Kocar, U. Karaagac, K. W. Chan, and E. Farantatos, "Impact of Inverter-Based Resources on Negative Sequence Quantities-Based Protection Elements," *IEEE Transactions on Power Delivery*, vol. 36, pp. 289–298, Feb. 2021.
- [9] W. Ren, M. Steurer, and T. L. Baldwin, "An effective method for evaluating the accuracy of power hardware-in-the-loop simulations," *IEEE Transactions on Industry Applications*, vol. 45, no. 4, pp. 1484–1490, 2009.
- [10] P. Vorobev, P.-H. Huang, M. Al Hosani, J. L. Kirtley, and K. Turitsyn, "High-fidelity model order reduction for microgrids stability assessment," *IEEE Transactions on Power Systems*, vol. 33, no. 1, pp. 874–887, 2018.
- [11] Y. A.-R. I. Mohamed, "Mitigation of dynamic, unbalanced, and harmonic voltage disturbances using grid-connected inverters with *lcl* filter," *IEEE Transactions on Industrial Electronics*, vol. 58, no. 9, pp. 3914–3924, 2011.
- [12] P. Kundur, "Power system stability," *Power system stability and control*, vol. 10, pp. 7–1, 2007.
- [13] N. Ainsworth, A. Hariri, K. Prabakar, A. Pratt, and M. Baggu, "Modeling and compensation design for a power hardware-in-the-loop simulation of an AC distribution system," in *2016 North American Power Symposium (NAPS)*, (Denver, CO, USA), pp. 1–6, IEEE, Sept. 2016.
- [14] K. Prabakar, B. Palmintier, A. Pratt, A. Hariri, I. Mendoza, and M. M. Baggu, "Improving the Performance of Integrated Power-Hardware-in-the-Loop and Quasi-Static Time-Series Simulations," *IEEE Transactions on Industrial Electronics*, pp. 1–1, 2020. Conference Name: IEEE Transactions on Industrial Electronics.
- [15] {IEEE PEL/SC}, "Hardware-in-the-Loop (HIL) Simulation Based Testing of Electric Power Apparatus and Controls," Standard {P2004}, I, Mar. 2017.
- [16] R. Teodorescu, F. Blaabjerg, M. Liserre, and P. Loh, "Proportional-resonant controllers and filters for grid-connected voltage-source converters," *IEE Proceedings - Electric Power Applications*, vol. 153, pp. 750–762, 2006.
- [17] W. Michiels, "Control of linear systems with delays," in *Encyclopedia of Systems and Control* (J. Baillieul and T. Samad, eds.), pp. 1–7, London: Springer London, 2019.
- [18] N. Olgac and R. Sipahi, "A practical method for analyzing the stability of neutral type lti-time delayed systems," *Automatica*, vol. 40, no. 5, pp. 847–853, 2004.
- [19] N. Pogaku, M. Prodanovic, and T. C. Green, "Modeling, analysis and testing of autonomous operation of an inverter-based microgrid," *IEEE Transactions on Power Electronics*, vol. 22, no. 2, pp. 613–625, 2007.